

REPRINT

N 1 S

IN-90-CR
119771

CIRCULATED

LATERAL SHOCK OF THE R AQUARII JET

J. M. HOLLIS

Space Data and Computing Division Code 930, NASA Goddard Space Flight Center, Greenbelt, MD 20771

J. A. PEDELTY

Biospheric Sciences Branch Code 923, NASA Goddard Space Flight Center, Greenbelt, MD 20771

AND

M. KAFATOS

Center for Earth Observing and Space Research, Institute for Computational Sciences and Informatics and Department of Physics,
George Mason University, Fairfax, VA 22030

Received 1996 October 28; accepted 1997 June 26

ABSTRACT

The R Aqr jet was observed with the VLA B-configuration at two epochs separated by ~ 13.2 yr. Comparison of the resulting 6 cm continuum images show that the radio jet has undergone a lateral counterclockwise rotation of $\sim 6^\circ$ - 12° on the plane of the sky. The model of jet parcels on independent trajectories is difficult to reconcile with these observations and leads us to consider a path-oriented jet (i.e., younger parcels follow the same path as older parcels). Comparison of the most recent radio image with a nearly contemporaneous *HST*/FOC ultraviolet image at ~ 2330 Å suggests that the ultraviolet emission lies along the leading side of the rotating radio jet. In conjunction with a proper motion analysis of the jet material that yields empirical space-velocity and resulting acceleration-magnitude relationships as a function of distance from the central source, we evaluate the observational results in terms of a schematic model in which the jet emission consists of plane-parallel isothermal shocks along the leading edge of rotation. In such a radiating shock, the ultraviolet-emitting region is consistent with the adiabatic region in the form of a high-temperature, low-density sheath that surrounds the cooled postshock radio-emitting region. Within the context of the schematic model, we obtain the temperatures, densities, and pressures within the preshock, adiabatic, and postshock regions as a function of distance from the central source; the physical parameters so derived compare favorably to previously published estimates. We obtain a total jet mass of $3.1 \times 10^{-5} M_\odot$ and an age of ~ 115 yr. We evaluate the model in the context of its density-boundary condition, its applicability to an episodic or quasi-continuous jet, and angular momentum considerations.

Subject headings: ISM: individual (R Aquarii) — ISM: jets and outflows — radio continuum: ISM — shock waves — ultraviolet: ISM

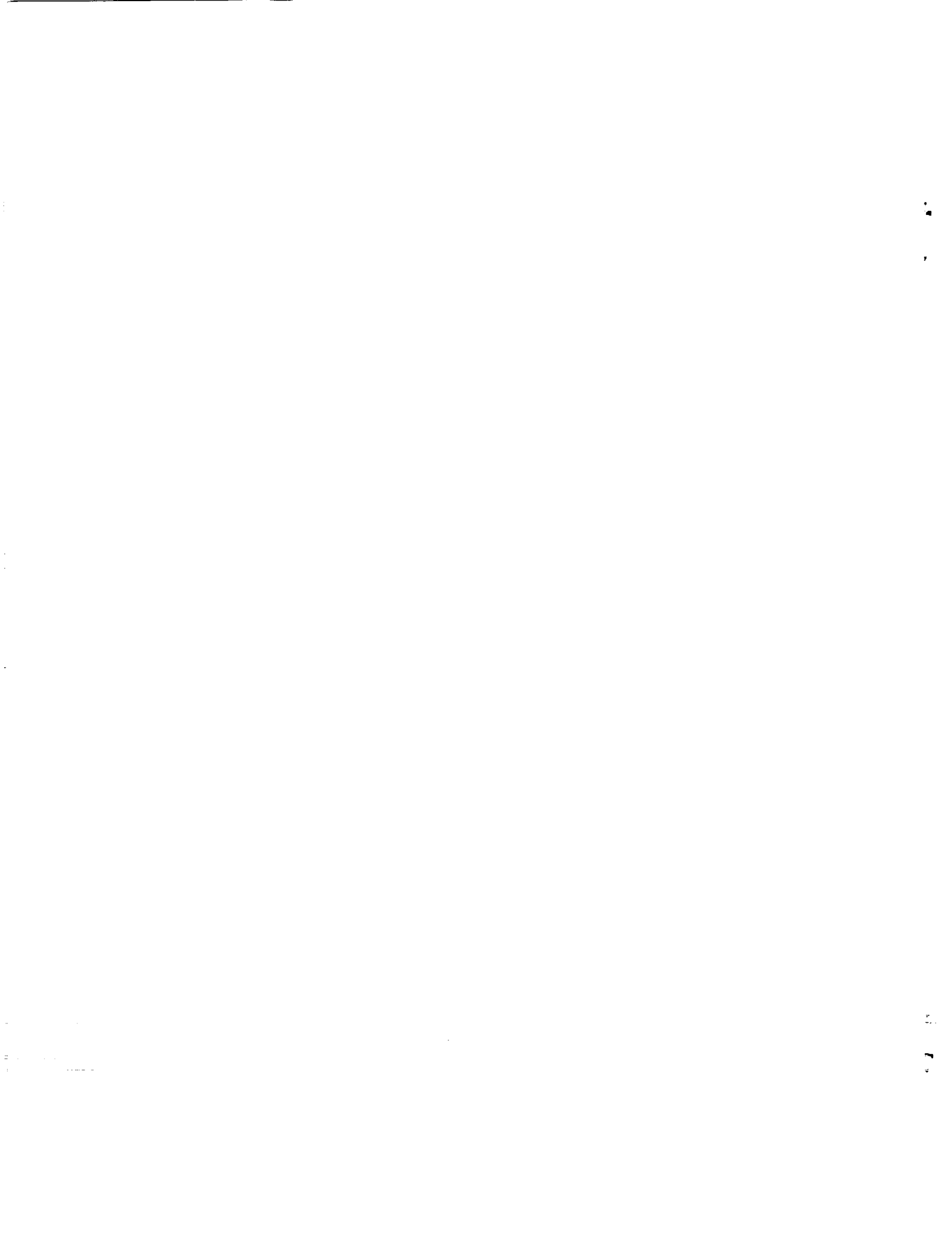
1. INTRODUCTION

R Aqr is a symbiotic stellar system comprised of a mass-losing $\sim 1.75 M_\odot$ (see Hollis, Pedelty, & Lyon 1997) Miralike long-period variable (LPV) of 387 days and a $\sim 1.0 M_\odot$ hot companion with a hypothetical accretion disk that is believed to give rise to symmetrical jetlike structures seen at ultraviolet, optical, and radio wavelengths (see Hollis et al. 1991; Solf & Ulrich 1985; and Hollis et al. 1985, respectively, and references therein). Proper-motion studies (Lehto & Johnson 1992; Hollis & Michalitsianos 1993; Hollis et al. 1997) show that such R Aqr radio and ultraviolet features represent an astrophysical jet as opposed to some other dynamical configuration; additionally, the criteria for a working definition of a radio jet (Bridle & Perley 1984) has also been shown to apply in the case of R Aqr (Kafatos, Michalitsianos, & Hollis 1986). The R Aqr binary orbit is suspected to be highly elliptical with estimates of eccentricity ranging from $e > 0.6$ to $e > 0.80$ (Hinkle et al. 1989; Kafatos & Michalitsianos 1982), and the binary period may be as long as ~ 44 yr (Willson, Garnavich, & Mattei 1981; Wallerstein 1986; Hinkle et al. 1989). The jet is believed to undergo episodic refueling at periastron when LPV wind capture would be enhanced or Roche lobe overflow occurs.

Comparison of 2 cm radio continuum imagery taken with the VLA and [O III] $\lambda 5007$ imagery taken with the

HST/FOC at nearly the same resolution ($\sim 0''.2$) shows that measurable spatial differences exist between the optical and radio emission regions in the inner $2''$ of the northeast (NE) R Aqr jet (Hollis, Dorband, & Yusef-Zadeh 1992). In this work, the [O III] emission region was found further removed radially from the central source than the 2 cm radio continuum region. This is just the opposite of that expected if excitation is caused primarily by a central ionizing source. However, in a shock-excited jet flowing radially outward, the higher ionization stages of a given atomic species would be formed further from the central source since ionization drops off behind the shock. Hence, it was suggested that thermal bremsstrahlung radiation in the radio region was a relic of the passing shock front as delineated by the [O III] emission—in this situation, the radio emission would increase as the gas is compressed behind the shock front, since the radio emission measure is proportional to the square of the increasing electron density.

On a larger scale, 6 cm radio continuum imagery taken with the VLA was also compared to [O III] $\lambda 5007$ imagery taken with the *HST*/FOC, which had been convolved with an elliptical Gaussian of the same size as the VLA limiting resolution ($\sim 0''.6$), showing that lateral (azimuthal) spatial differences exist along the entire $\sim 12''$ extent of the eastern edge of the NE jet (Hollis & Michalitsianos 1993). In this work, it was suggested that the lateral spatial differences



result from shock excitation in which the shock front [O III] line emission appears on the leading eastern edge of the jet relative to the postshock thermal radio emission. This global jet morphology was interpreted as having been caused by precession of a rotating collimated stream as it encounters ambient circumstellar material.

Proper-motion studies of the R Aqr jet in 6 cm radio-continuum emission (Lehto & Johnson 1992; Hollis & Michalitsianos 1993) and in ultraviolet [O II] $\lambda 2470$ line emission (Hollis et al. 1997) show that the bulk of the jet motion flows radially away from the LPV but that there is also a significant component orthogonal to the radial flow. These previous studies develop empirical velocity and acceleration magnitude relationships as a function of distance from the LPV. Velocity magnitudes differ between the radio and ultraviolet emission components, but both characteristic velocity magnitude functions smoothly increase with increasing distance from the LPV. Further, the ultraviolet components show nonlinear acceleration, while the radio components show constant acceleration. On the other hand, both the radio and ultraviolet jet kinematics suggest a period of $\sim 40\text{--}44$ yr between enhanced material ejection. Since these two different manifestations of the jet, as represented by the radio and ultraviolet emission regions, are in proximity but not cospatial, Hollis et al. (1997) concluded two different streams of gas exist with a distinct boundary between them.

In this work, we are motivated to explain the results of a comparison of VLA observations of the R Aqr jet which are separated by 13.2 yr. The comparison shows that there is an apparent lateral counterclockwise (CCW) motion of the jet on the sky. This motion is difficult to reconcile with independent trajectories for the gas parcels in the R Aqr jet. Thus, we are led to consider a path-oriented jet in which younger parcels follow the same path as older parcels. Since the ambient medium of the heavy jet is a less dense nebula at $\sim 10^4$ K (Hollis et al. 1987), we adopt a simplified, two-dimensional, isothermal shock model in which the shocked gas of the jet cools rapidly to $\sim 10^4$ K because of the higher densities involved (see Kafatos, Michalitsianos, & Hollis 1986). This schematic model assumes a biconical geometry for the R Aqr jet in which the ultraviolet-emitting region is contained in a sheath around the radio-emitting core. In this radiating shock (see Spitzer 1978 for a schematic diagram), the ultraviolet data sample the adiabatic region, and the radio data sample the cooled postshock region. The relevant physical parameters derived for the model (e.g., temperature, density, velocity, and mass and age of the jet) agree favorably with previously published estimates. We find the model violates no known physical constraints on the R Aqr system and we offer an observational test. We feel it is premature to attempt to generate numerical solutions of the 3-dimensional MHD equations; instead, we are intrigued at how much seems to be explained within the context of our schematic model.

Finally, we caution the reader that our model discussion is somewhat difficult to follow without frequently consulting the figures regarding the geometry arguments.

2. OBSERVATIONS

2.1. VLA Imagery

R Aqr was observed on 1982 September 26 and again on

1995 December 9 with the NRAO¹ Very Large Array in the B configuration. In 1982, 27 antennas were employed at 4885 MHz (~ 6 cm), utilizing an intermediate-frequency (IF) bandwidth of 50 MHz. The 1995 observations also employed 27 antennas and were made while the VLA was operating in phased-array mode as part of a session with the Very Long Baseline Array (VLBA). Two IFs were used, but the combination of VLA constraints and VLBA requirements meant that both were set to operate at 4985 MHz with 50 MHz bandwidths. As these are not independent signals, the IFs were not averaged in the final processing. For both 1982 and 1995 observations, scans of R Aqr were interleaved with scans of the quasar 2345–167 (equivalently 2348–165 in J2000 coordinates) for phase-calibration purposes. In 1982, the duration of an R Aqr scan was ~ 12 minutes on-source, and the duration of the phase calibrator scan was ~ 2 minutes on-source; in 1995, this duty cycle was reduced to ~ 4.5 minutes for R Aqr and ~ 1.5 minutes for the phase calibrator. In 1982, a total of 31 scans were performed on R Aqr, and 32 scans were performed on the calibrator; in 1995, the R Aqr scans totaled 55 and the calibrator scans totaled 67.

Observations of 3C 48 were made to establish the absolute flux calibration scale by assuming 3C 48 had flux densities of 5.607/5.502 Jy at the frequencies used in the 1982/1995 observations. These flux density values are obtained from the 1990 VLA calibrator manual and are slightly different than those used by Kafatos, Hollis, & Michalitsianos (1983), who originally published the 1982 data. Since 3C 48 is resolved, only visibilities with baselines less than $40\text{ k}\lambda$ were used for this purpose. The bootstrapped flux densities of the calibrator for the two epochs were 3.133(20)/2.907(9) Jy. The calibrated visibilities from each epoch were gridded onto 1024 by 1024 arrays and were then Fourier transformed before image CLEANing (a particular method of sidelobe removal; see Clarke 1981; and Cornwell & Braun 1989). The AIPS task IMAGR was employed for this task, and clean boxes were set to include all radio sources detected within the $\sim 9'$ FWHM primary beam. Both observing sessions yielded very similar samplings of the u-v plane, and identical restoring beams ($1''.67$ by $1''.25$ with a major axis position angle of 0°) were used for both epochs. The 1982 image was precessed to J2000, and a further correction for the stellar proper motion was made by aligning the peaks of the two epochs using the AIPS task LGEOM. The resulting images for 1982 and 1995 have rms sensitivities of 19 and 26 μ Jy, respectively, and are shown superimposed in Figure 1 (Plate 5).

2.2. HST/FOC Image

R Aqr was observed on 1994 September 29 (15.5 minute exposure) with the HST/FOC in the f/96 mode of operation using the F2ND ($\Delta m = 2$) and F231M filters (~ 2330 Å center, 230 Å FWHM). These data were taken after the COSTAR correction mission, which makes the HST/FOC f/96 mode of operation effectively an f/151 instrument owing to the negative lens correction, yielding an astrometrically verified pixel size of 0.01435 arcsec² (Nota, Jedrzejewski, & Hack 1995). The predominant spectral features in the F231 filter bandpass are C II] near 2326 Å and [O II]

¹ The National Radio Astronomy Observatory is operated by Associated Universities, Inc., under cooperative agreement with the National Science Foundation.

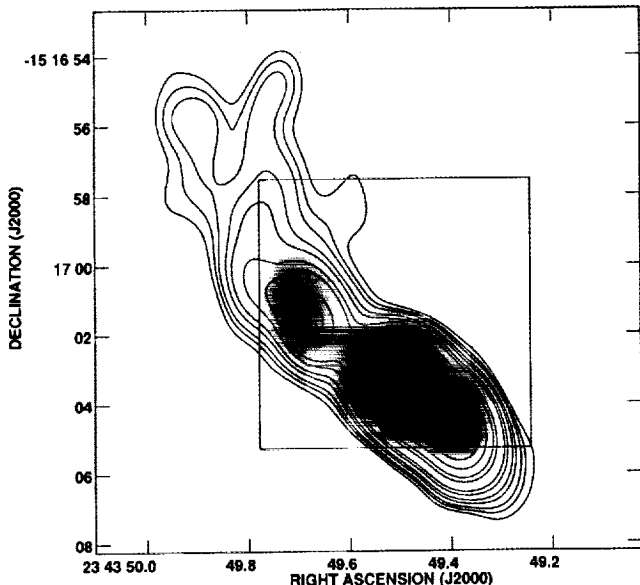


FIG. 2.—Gray-scale of the 1994 *HST*/FOC ultraviolet image ($\sim 2330 \text{ \AA}$) that has been convolved with a 1.67×1.25 FWHM Gaussian to permit same-resolution comparison with a 6 cm contour plot of the 1995 6 cm VLA image of the R Aqr jet. Radio contours are 0.08, 0.12, 0.16, 0.24, 0.32, 0.36, 0.64, 1.20, 1.60, 2.56, 3.84, and $5.12 \text{ mJy beam}^{-1}$, and the peak radio flux is $\sim 10.0 \text{ mJy beam}^{-1}$. The box delimits the field of view of the *HST* image relative to the VLA image. Comparison of the radio image with the nearly contemporaneous *HST*/FOC ultraviolet image suggests that the ultraviolet emission could encompass the radio emission in a sheath if a shock model applies.

near 2470 \AA . The 512×512 data frame was flat-fielded and geometrically corrected with standard IRAF STSDAS routines; the resulting diffraction-limited image ($\sim 0.2''$ resolution) is shown superimposed on the much coarser resolution (1.67×1.25 beam) radio data in Figure 1. Therefore, it is likely that the *HST* image in Figure 1 shows the true morphology of the R Aqr jet. Figure 2 shows the 1994 *HST* ultraviolet image convolved with a 1.67×1.25 FWHM Gaussian and superimposed on the nearly contemporaneous 1995 radio data for same-resolution comparison.

3. MODEL DEVELOPMENT AND COMPARISON WITH OBSERVATIONS

The Figure 1 morphology of the superimposed 6 cm continuum VLA images taken in 1982 and 1995 shows that the NE R Aqr radio jet has undergone a lateral CCW rotation

on the plane of the sky. The observed angular displacements over the course of the 13.2 yr range from $\sim 6^\circ$ for features closer to the LPV to $\sim 12^\circ$ for features at the jet extremities. Proper-motion studies of four radio jet features C2, A, B, and D relative to the LPV, along with relative proper-motion studies of ultraviolet jet components NE1 and NE2, are given in Table 1. We find that a CCW angular velocity of $\sim 0.5^\circ \text{ yr}^{-1}$ provides the best fit to the observed angular displacements of Table 1 features.

3.1. Overview of Modeling Approach

The CCW motion of the jet axis leads us to consider a path-oriented jet and its consequences in terms of successive isothermal shocks along the jet axis. The radio jet is at 10^4 K (see, e.g., Hollis et al. 1985), and the large-scale optical nebula (e.g., see, Solf & Ulrich 1985) and its radio counterpart (Hollis et al. 1987) in which the jet is embedded are at 10^4 K , thereby justifying an isothermal approximation. We will assume that the jet is conical and that the ultraviolet emission (adiabatic-shock region) surrounds the radio emission (postshock region at 10^4 K) as shown in Figure 3. From a proper-motion analysis of Table 1 data, we will develop empirical space-velocity and acceleration-magnitude relationships as functions of distance from the central source (hereafter the LPV) for the ultraviolet and radio jet material and then derive the corresponding density relationships by invoking the mass-continuity equation along the jet. We will then obtain the temperature of the adiabatic shock region as a function of distance from the LPV from isothermal shock theory. While Figure 3 shows the jet in three dimensions, our shock model is actually two-dimensional, characterized by the jet axial coordinate s and a whole series of independent x_s . Each x is defined by the idealized one-dimensional disturbance propagating across the shock front and lies in the direction of the space-velocity of the jet (V_j) as shown in Figure 3. Figure 3 shows only one of the successive shock fronts for clarity and does not show x explicitly, but x can be inferred from the expanded inset (i.e., an idealized schematic diagram of a radiating shock; see also Spitzer 1978). Moreover, note that Figure 3 shows a three-dimensional sheath for the UV emission along the leading (moving) edge of the radio cone. We are not calculating a three-dimensional shock model that would rightly result in an oblique shock geometry due to the curvature of the sheath surface; we are simply going to apply our model to the “crest” of the sheath (as defined by the impinging space velocity) and see if it approximates the

TABLE 1
MOTION OF UV AND RADIO FEATURES OF THE NE JET RELATIVE TO THE LPV

NE Jet Feature (1)	PA of Feature ^a (deg) (2)	Distance of Feature ^a (arcsec) (3)	μ Rel to LPV ^a (arcsec yr ⁻¹) (4)	PA for μ ^a (deg) (5)	V_μ ^b (km s ⁻¹) (6)	V_{LOS} ^c (km s ⁻¹) (7)	V_j ^d (km s ⁻¹) (8)
LPV	0.00	0.000	...	0.0	0	0.0
NE1 (UV)	45	0.83	0.031	45	35.7	-10	37.1
NE2 (UV)	45	4.34	0.204	61	235.2	-25	236.5
C2 (RADIO)	55.9	0.82	0.047	69	54.2	-10	55.1
A (RADIO)	47.5	3.70	0.096	62	110.7	-25	113.5
B (RADIO)	37.5	7.57	0.145	77	167.2	-29	169.7
D (RADIO)	23.1	9.20	0.165	45	190.2	-35	193.4

^a Data taken from Hollis et al. 1997 for ultraviolet features and Lehto & Johnson 1992 for radio features.

^b Velocity in the plane of the sky resulting from proper motion of jet component relative to the LPV at 250 pc.

^c Line-of-sight velocity relative to the rest frame of the LPV; derived from optical observations of Solf & Ulrich 1985.

^d Magnitude of the true space velocity (V_j) of a jet-emission component (see Fig. 3).

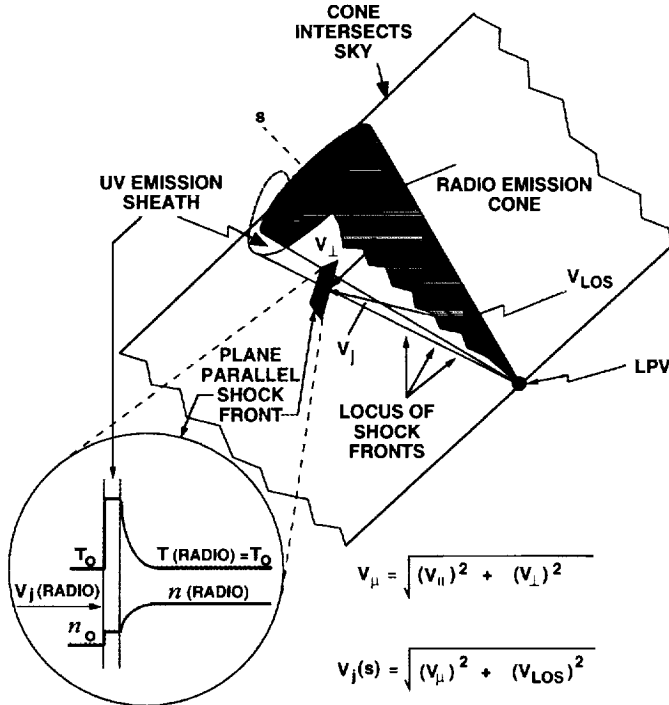


FIG. 3.—Idealized schematic of the shock-model geometry suggested by the observations. The plane of the paper defines the sky plane in this schematic whose scale is exaggerated in order to be illustrative. The radio emission fills the cone whose s axis (dashed line) is tilted out of the sky plane toward the observer by $\sim 10^\circ$. The UV emission lies on the leading edge of the shock and surrounds the relic radio emission (see Fig. 2). The sheath being squeezed by the shock process causes higher velocities to prevail for ultraviolet material as compared to the relic radio-material shock velocities. The vector V_μ lies in the plane of the sky and represents the velocity resulting from the proper motion of a jet component with respect to the LPV at an assumed distance of 250 pc. The velocities V_{\parallel} and V_{\perp} lie in the plane of the sky and are orthogonal components of V_μ , representing vectors parallel and perpendicular, respectively, to the direction of the s axis projected onto the plane of the sky. The velocity V_μ (equivalently components V_{\parallel} and V_{\perp}) and the line-of-sight radial velocity (V_{LOS}) form an orthogonal three-dimensional coordinate system that defines the true space velocity (V_j) of a jet-emission component (see eqs. [3] and [4]). The text develops the model of multiple plane-parallel shocks in the direction of an ensemble of V_j vectors that are functions of s , but for clarity, only one V_j vector is shown here.

observations. In doing so, we arrive at plots of physical parameters in terms of the parameter s . Such plots are potentially misleading in the sense that we will string together a whole series of simple isothermal shock results as parameterized by s . These results at each s are truly independent, but the physical parameters plotted against s give the appearance of a smooth model which we caution the reader not to misinterpret. Finally, we will use the model to determine the mass and age of the jet.

3.2. Development of the Model

As can be determined from Table 1 data, the bulk of the jet motion is in a direction radially away from the LPV (see cols. [2] and [5]). However, Table 1 data also support the current observations in Figure 1 that show a significant motion component orthogonal to the radial direction. Using Table 1 data, radio components C2, A, B, and D follow an empirical proper motion magnitude relationship,

$$\mu(\text{radio}) = 0.0492(s_{\text{SKY}})^{0.55} \text{ arcsec yr}^{-1}, \quad (1)$$

while the ultraviolet components NE1 and NE2 follow

$$\mu(\text{UV}) = 0.0383(s_{\text{SKY}})^{1.14} \text{ arcsec yr}^{-1}, \quad (2)$$

where s_{SKY} is the observed distance in arcseconds from the LPV (in terms of Fig. 3 geometry, s_{SKY} would be the projection of s onto the plane of the sky), and the μ position angle (i.e., direction) for each feature is given in Table 1. Equations (1) and (2) are plotted in Figure 4 and are obviously independent of the distance to R Aqr. The pronounced difference in the exponents of equations (1) and (2) implies that the radio and ultraviolet emissions cannot originate from the same gaseous region.

Using equation (1), the magnitude of vector V_μ can be determined for radio emission components (see Table 1); this vector lies in the plane of the sky and represents the velocity resulting from the proper motion of a jet component with respect to the LPV at an assumed distance of 250 pc (Whitelock 1987). Using equation (2), the magnitude of V_μ can similarly be determined for ultraviolet emission components (see Table 1). Moreover, optical emission-line observations (Solf & Ulrich 1985) of the NE jet corresponding to positions of C2/NE1, A/NE2, B, and D yield line-of-sight (LOS) radial velocities (V_{LOS}) with respect to the LPV as shown in Table 1. The orthogonal velocities V_μ and V_{LOS} yield jet-space velocities, V_j , whose magnitudes are shown in Table 1. Radio and ultraviolet components follow space-velocity magnitude relationships

$$V_j(\text{radio}) = 57.8 s^{0.55} \text{ km s}^{-1} \quad (3)$$

$$V_j(\text{UV}) = 45.7 s^{1.12} \text{ km s}^{-1}, \quad (4)$$

where the distance s shown in Figure 3 is the true space-distance of the emission component from the LPV and is expressed here in arcseconds for convenience (equivalently, $1'' = 3.64 \times 10^{15} \text{ cm}$ at 250 pc). Note that the distance parameter s is used to express the velocity magnitude relationships without regard for velocity direction (see Fig. 3). Equations (3) and (4) are plotted in Figure 5 (upper panel). The inclination of the space-velocity vectors to the plane of the sky (0° defines the plane and 90° is toward the observer) averages to $\sim 10.7^\circ \pm 3^\circ$ for all radio and ultraviolet components. Moreover, the space-velocity vectors

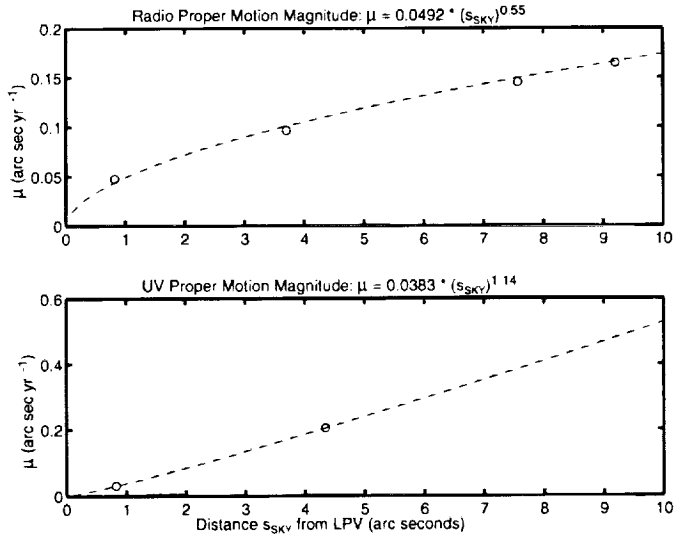


FIG. 4.—Top: Plot of radio-component proper motion as a function of observed distance on the sky relative to the LPV. Bottom: Plot of ultraviolet-component proper motion as a function of observed distance on the sky relative to the LPV. Data for this figure are taken from Table 1.

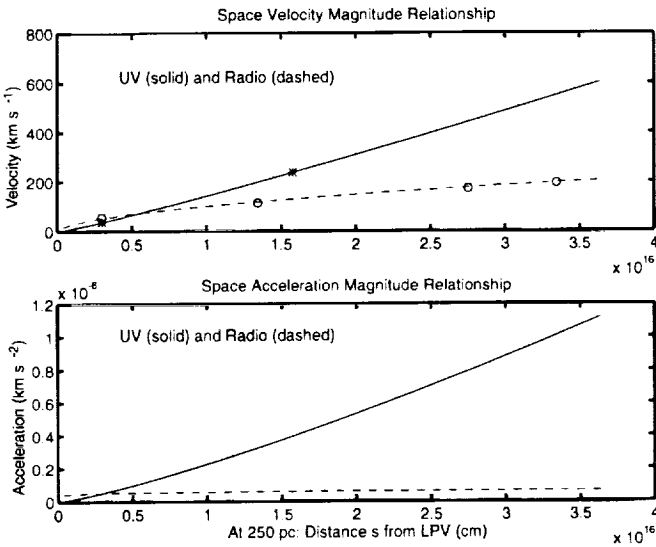


FIG. 5.—*Top:* Plot of space velocities for radio and ultraviolet components as a function of distance s relative to the LPV. *Bottom:* Plot of space accelerations for radio and ultraviolet components as a function of distance s relative to the LPV. The space-velocity and acceleration results are dependent on Table 1 data, the distance to R Aqr, and observed line-of-sight radial velocities (see text).

have an average position angle direction $\sim 60^\circ \pm 12^\circ$ as determined from the proper-motion position angles in Table 1. Thus, the bulk space motion of the NE jet is toward the observer and east by northeast, suggesting that both the radio and ultraviolet components are in proximity.

Radio and ultraviolet components follow the space acceleration-magnitude relationships

$$a_j(\text{radio}) = 5.03 \times 10^{-8} s^{0.10} \text{ km s}^{-2} \quad (5)$$

$$a_j(\text{UV}) = 6.44 \times 10^{-8} s^{1.24} \text{ km s}^{-2}, \quad (6)$$

where s is the true space distance from the LPV expressed in arcseconds. Equations (5) and (6) are plotted in Figure 5 (*lower panel*). Note $a_j(\text{radio})$ varies by only $\sim 25\%$, while $a_j(\text{UV})$ varies by a factor of 18 over the range $0''.9 \leq r \leq 9''.2$. Since these two different manifestations of the jet as represented by the radio and ultraviolet emissions are undergoing acceleration that cannot be accounted for by radiation pressure alone, Hollis et al. (1997) have suggested that the likely propulsive force results from MHD effects in accordance with the model of Koupelis & Van Horn (1988). As noted for equations (1) and (2), and again here for equations (5) and (6), the pronounced difference in the exponents suggests that there are two streams of gas with a distinct boundary between them. This assumption is valid if the mean free paths of thermal particles are short compared to the linear sizes of the regions involved, which would preclude any appreciable diffusion of one gas stream into the other (see Dyson & Williams 1980). We will show that the ultraviolet-emitting region is characterized in the extreme by a high-temperature ($\sim 3 \times 10^5$ K) and low-density ($\sim 100 \text{ cm}^{-3}$) combination that provides a thermal mean free path of $\sim 10^{13} \text{ cm}$, or, equivalently, $\leq 0''.005$ (at 250 pc); such a scale size is less than the resolution of the ultraviolet data and meets the condition for little appreciable diffusion into the cooler, more dense radio region that possesses a shorter thermal mean free path in comparison.

The morphology exhibited by the NE jet has been previously modeled as a garden hose with each parcel of

material ejected free to follow its own unique trajectory (Hollis & Michalitsianos 1993). However, based on the observations in Figure 1 and the dichotomy of velocity-magnitude relationships as expressed in equations (1) and (2), we are observationally constrained to assume that a continuous-jet model applies where new matter flows along the path previously taken by older material; quite possibly the path itself could experience precessional effects if a path-oriented model is correct. In this jet model, the equation of mass conservation is

$$\rho_j(s)V_j(s)A_j(s) = K_1, \quad (7)$$

where the total particle-jet density, ρ_j , the jet-space velocity, V_j , and jet cross-sectional area, A_j , are functions of the distance s from the LPV and K_1 is a constant. Since the radio-jet data have coarse resolution, we use the corresponding high-resolution ultraviolet observations (see Fig. 1), which suggest that a simple configuration for the jet is that of a right circular cone with an opening apex angle of $2\theta \sim 16^\circ$, and, hence, equation (7) can be written

$$\rho_j(s)V_j(s)s^2 = K_2, \quad (8)$$

where we have used $A_j(s) = \pi(s\theta)^2$ and K_2 is a constant. We assume that ultraviolet emission could be coming from a hotter, lower density sheath surrounding the radio jet (see Figs. 2, 3, and Leahy & Taylor 1987). An ultraviolet-emission sheath being squeezed by the shock process could explain the general condition shown in Table 1 and equations (3) and (4) that higher velocities prevail for ultraviolet material as compared to radio material in close proximity. For a sheath, $A_j(s) = \pi s^2 2\theta \Delta\theta$, and equation (8) would still apply. The density relationships for both the radio and ultraviolet emissions immediately follow from equations (3), (4), and (8):

$$n_j(\text{radio}) = K(\text{radio}) s^{-2.55} \text{ cm}^{-3} \quad (9)$$

$$n_j(\text{UV}) = K(\text{UV}) s^{-3.12} \text{ cm}^{-3}, \quad (10)$$

where s is the true space distance from the LPV expressed in arcseconds, $K(\text{radio})$ and $K(\text{UV})$ are appropriate constants to be determined, and we have used the relation $\rho_j = n_j \mu m_H$ (where μ is the mean atomic mass per particle and m_H is the mass of the hydrogen atom).

To determine the constants in equations (9) and (10), we must estimate the mass-losing LPV wind density, ρ_w , at the position of the white dwarf. The appropriate relationship is

$$\rho_w = n_w \mu m_H = \dot{M}/(4\pi d^2 v_w) \text{ g cm}^{-3}, \quad (11)$$

where \dot{M} is the mass-loss rate of the LPV, v_w is the LPV wind velocity, d is the distance between the white dwarf and the LPV, $\mu \sim 0.61$, and the factor of 4π results from the usual assumption of spherical symmetry. The mass-loss rate from the LPV has been estimated at $\sim 2.7 \times 10^{-7} M_\odot \text{ yr}^{-1}$ from radio data (Hollis et al. 1985; see also Michalitsianos, Kafatos, & Hobbs 1980), although Michalitsianos et al. (1988) suggest that this may be an underestimate. Mass transfer from the LPV to the secondary is necessary for the formation of the accretion disk and is facilitated if the orbital eccentricity, e , is large enough to cause Roche lobe overflow. The criterion in such a binary system is $a(1 - e) \sim 2R_{\text{LPV}}$, where a is the semimajor axis (Haynes, Lerche, & Wright 1980) and $R_{\text{LPV}} \sim 300 R_\odot$. Assuming an orbital period of 44 yr and a total system mass of $2.75 M_\odot$ (Hollis et al. 1997), $a \sim 2.5 \times 10^{14} \text{ cm}$. Thus, we take $e \sim 0.85$ to ensure that Roche lobe mass transfer occurs and

obtain a periastron distance of 4×10^{13} cm, which we use as an approximation for d in equation (11). Typically, LPVs have radiatively driven asymptotic wind velocities in the range $5\text{--}20 \text{ km s}^{-1}$ (Omont 1991). On the other hand, for our assumed $d \sim$ twice the LPV radius, dust may not yet be formed, but shocks or pulsations in the LPV envelope could drive material outward at velocities no larger than 5 km s^{-1} (Reid & Menten 1997). In either case, adopting $v_w \sim 5 \text{ km s}^{-1}$ for R Aqr seems a reasonable compromise. Near periastron, it is highly unlikely that LPV mass loss is spherical, and, therefore, we make the assumption that all of the mass loss gets used up in a bicone with apex angle of $2\theta \sim 16^\circ$ (see assumptions for eq. [8] above). The resultant solid angle $\Omega = 2\pi(\theta)^2$ replaces the factor of 4π in equation (11) which yields $n_w \sim 1.6 \times 10^{11} \text{ cm}^{-3}$ at $d \sim 4 \times 10^{13}$ cm, providing the initial density condition for the determination of $K(\text{radio}) \sim 1.6 \times 10^6$ and $K(\text{UV}) \sim 1.2 \times 10^5$. Thus, equations (9) and (10) now provide the run of ultraviolet-region and radio-region densities along the jet (see Fig. 6, *lower panel*). The assumption that all the mass loss goes into the jet is certainly questionable and, if anything, would result in an overestimation of density. However, we note Reid & menten (1997) have shown from observational data that a singly evolving LPV has a typical density of $\sim 1.5 \times 10^{12} \text{ cm}^{-3}$ at a radius of 4.8×10^{13} cm; these parameters were derived assuming spherical symmetry and, as such, support our derived boundary conditions.

For an isothermal shock model, we assume that the radio emission all along the jet is $T_f(\text{radio}) = 10^4 \text{ K}$ and that this condition holds for the temperature of the ambient medium, T_o . Since the ultraviolet-emission region is the adiabatic-shock region (see Fig. 3), we know the ambient medium density $n_o = n_f(\text{UV})/4$ (see Fig. 6, *lower panel*). Further, it can be shown that the peak temperature in the thin adiabatic shock region is

$$T_f(\text{UV}) = 3n_f(\text{radio})T_f(\text{radio})/[4n_f(\text{UV})] \text{ K} \quad (12)$$

which is shown in Figure 6, (*upper panel*). Using the equation of state $P = \rho kT/\mu m_H$ (k is the Boltzman constant), we

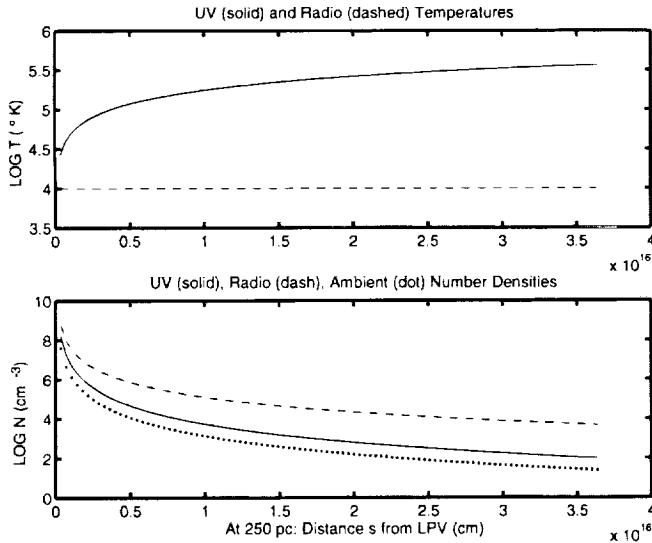


FIG. 6.—*Top:* Plot of temperature for the thin adiabatic shock region (UV-emitting region) as a function of distance s relative to the LPV. *Bottom:* Plot of number densities for the preshock (ambient), adiabatic (UV-emission), and postshock (radio-emission) regions as a function of distance s relative to the LPV. This figure is based on an isothermal shock model of 10,000 K.

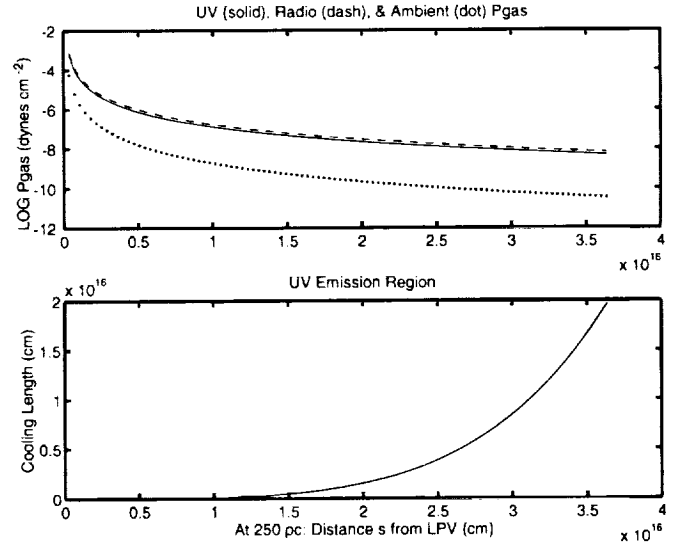


FIG. 7.—*Top:* Plot of gas pressure for the preshock (ambient), adiabatic (UV-emission), and postshock (radio-emission) regions as a function of distance s relative to the LPV. This figure is based on an isothermal shock model of 10,000 K. *Bottom:* Plot of cooling length for the adiabatic shock region (UV-emitting region) as a function of distance s relative to the LPV.

can determine the run of pressures in the ambient, adiabatic, and postshock regions of the radiating shock (see Fig. 7, [*upper panel*]). Moreover, in the rest frame of the shock, the model upstream Mach number function

$$M = \sqrt[n_f(\text{radio})/n_o]{ } \quad (13)$$

is shown in Figure 8, (*upper panel*). For comparison, Figure 8 also shows the Mach numbers from the radio data in the rest frame of the LPV; that is, the shock speeds (see Fig. 3) as represented by space velocities of radio features C2, A, B,

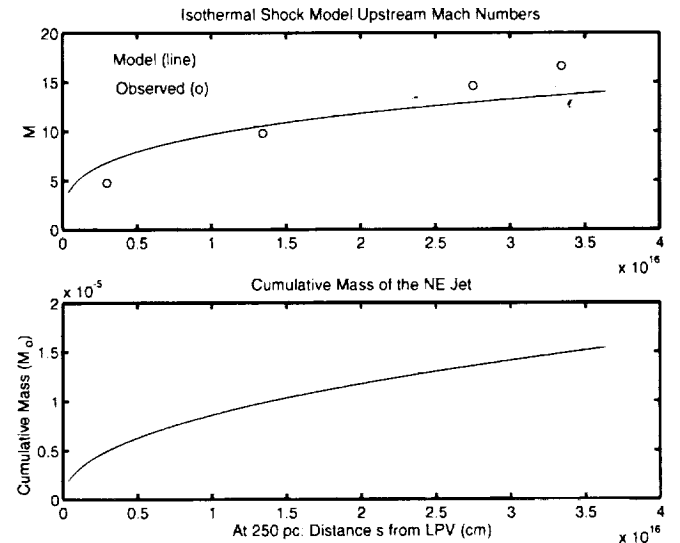


FIG. 8.—*Top:* Plot of Mach numbers as a function of distance s relative to the LPV. The solid line is based on an isothermal shock model of 10,000 K, and the upstream Mach numbers were calculated in the rest frame of the shock. Circles represent Mach numbers determined from the motion of observed radio components relative to the fixed rest frame of the LPV (see Table 1 data) for an assumed distance to R Aqr of 250 pc and utilizing an isothermal sound speed of 11.6 km s^{-1} . *Bottom:* Plot of cumulative mass in the NE jet as a function of distance s relative to the LPV. Total jet mass for both the NE and SW jets would be double the end value shown here.

and D shown in Table 1 divided by the isothermal sound speed of 11.6 km s^{-1} . The Mach number determinations in the two reference frames reasonably compare as they should (see, e.g., Dyson & Williams 1980; Spitzer 1978). Additionally, in Figure 7 (*lower panel*), we have used the model to calculate the radiative cooling length as a function of distance in the adiabatic shock region, showing that these lengths are rather large, providing explicit confirmation that the region does not radiate. The electron density in the radio-emitting regions can be determined from the following:

$$n_e(\text{radio}) = n_j(\text{radio})(\mu + 2)/5 \text{ cm}^{-3} \quad (14)$$

which yields electron number densities of 1.5×10^6 , 3.0×10^4 , and $4.9 \times 10^3 \text{ cm}^{-3}$ for radio features C2, A, and B, respectively; these values reasonably compare with electron densities derived from observations: $C2 \sim 4 \times 10^5 \text{ cm}^{-3}$ (Kafatos, Michalitsianos, & Hollis 1986), and $A \geq 2 \times 10^4 \text{ cm}^{-3}$ and $B \sim 7 \times 10^3 \text{ cm}^{-3}$ (Hollis et al. 1985).

We can estimate the total mass of the NE and SW jets by integrating the radio density function within the right circular cone of one jet and doubling the result. As a function of distance, s , a volume element of the cone is $dV = \pi\theta^2 s^2 ds$. Figure 8, (*lower panel*) shows the cumulative mass of the NE jet as a function of distance s relative to the LPV, and we obtain a jet total mass, $M_{\text{TOT}} \sim 3.1 \times 10^{-5} M_{\odot}$. The ratio M_{TOT}/\dot{M} yields a timescale of $\sim 115 \text{ yr}$, which is comparable to the observed age of the oldest radio jet components. For example, Lehto & Johnson (1992), using a constant-acceleration model, obtained ages of 95.6 and 106.8 yr for features B and D, respectively, while Hollis & Michalitsianos (1993), using a slightly different constant-acceleration model analysis, obtained corresponding ages of 135.2 and 120.2 yr for these same radio features. Enhancement of the mass loss during periastron either through Roche-lobe overflow or asymmetric capture due to the presence of the hot companion is a reasonable expectation. If we assume that the jet features are not emitted continuously but are ejected in episodic outflows occurring at periastron (see Kafatos, Michalitsianos, & Hollis 1986) which last $\sim 1 \text{ yr}$ (Kafatos & Michalitsianos 1982), it may well be that near periastron, enhanced mass loss from the LPV is $\sim 10^{-5} M_{\odot} \text{ yr}^{-1}$ (see Fig. 1 of Schild 1989), appreciably higher than the quiescent LPV wind loss rate of $\sim 2.7 \times 10^{-7} M_{\odot} \text{ yr}^{-1}$ as determined by Hollis et al. (1985). For episodic outflows, the enhanced wind loss rate averaged over the $\sim 44 \text{ yr}$ orbital period would be reduced to a value comparable to the quiescent wind loss rate for the case of continuous outflow. Thus, the episodic outflow case would also yield a similar age of $\sim 100 \text{ yr}$ for the jet.

4. MODEL-RELATED ISSUES

4.1. Density-Boundary Condition and LPV Mass Loss

We view our density-boundary condition and our assumption that all the mass loss from the LPV goes into the formation of the jet as the two most tenuous aspects of the isothermal-shock model. However, we derived a density-boundary condition value that is down by an order of magnitude from values taken from observations (see Reid & Menten 1997) at the same distance as the R Aqr binary separation at periastron. Without assuming some density-boundary condition, we cannot make any progress. However, the final model result gives us a jet age that is

similar to ages published previously (see e.g., Lehto & Johnson 1992; Hollis & Michalitsianos 1993) and this suggests that our assumptions are probably not unrealistic.

4.2. Quasi-continuous, Path-oriented Jet

Another concern is whether the jet is episodically or continually ejecting parcels of gas. Obviously, our model does not accommodate the former since the physical parameters shown in Figures 6–8 appear to be smooth functions. For a highly eccentric orbit with $e \geq 0.8$ (see Kafatos, Michalitsianos & Hollis 1986; Hinkle et al. 1989), the time at periastron would be relatively short to pick up new material for the accretion disk—it would take $\sim 2.2 \text{ yr}$ to go from one endpoint of the latus rectum to the other and the rest of the time, $\sim 41.8 \text{ yr}$, could be expended sending this material out into the jet. Hence, a quasi-continuous jet could result with observable enhancements at periastron as is suggested from observations (Lehto & Johnson 1992; Hollis & Michalitsianos 1993; Hollis et al. 1997). Moreover, the path-oriented aspect of the jet is reasonable as long as the time scale for filling the path with ambient material is longer than the presumed 44 yr period between new enhancements of outflow material. In terms of the model we propose, Figure 7 shows that the pressure in the quasi-continuous jet is greater than the ambient, ensuring that there would be no filling by ambient material at all. However, the observations can be interpreted as a series of discrete parcels expelled at orbital intervals. After being ejected 44 yr previously, a parcel will have expanded to a radius $R \sim 2 \times 10^{15} \text{ cm}$ and will be travelling at $\sim 100 \text{ km s}^{-1}$. The timescale for filling the path after such a parcel moves on would be $R/C_s > 60 \text{ yr}$ where the sound speed $C_s \sim 10 \text{ km s}^{-1}$; this filling timescale is a minimum since we have assumed the parcel moves on leaving a vacuum behind, a highly unlikely situation.

4.3. Other Models

Clearly our two-dimensional, smooth schematic model should be considered only an initial attempt to explain a number of diverse observations in the ultraviolet, optical, and radio regimes—in particular, Figure 1 radio and ultraviolet data that show the apparent lateral rotation of the jet over a 13.2 yr timespan. A full three-dimensional MHD approach is probably beyond the scope of the extant data for the R Aqr jet. As mentioned previously, we consider the model of Koupelis & Van Horn (1988) as worthy of pursuit in the case of R Aqr. In this model, a parcel of ejected dust and gas is emitted along the rotation axis of the rotating star–accretion disk system which anchors a strong magnetic field that is frozen into the rotating parcel as well as the central source; since the parcel is free to expand, its rotation rate decreases, and the field is twisted into a helix (observed in the R Aqr jet by Hollis et al. 1997); the consequent increase in the azimuthal component of the magnetic field builds up a strong magnetic pressure behind the parcel and accelerates it along the jet (acceleration was verified in the R Aqr jet by Lehto & Johnson 1992; Hollis & Michalitsianos 1993; and Hollis et al. 1997). Parcel expansion would account for transverse displacement that increases for increasing distance s relative to the LPV. However, our observations in the present work show there is a CCW preference for some lateral motion which is not included in the Koupelis & Van Horn (1988) model, and we believe it derives from path-oriented precession.

4.4. Regarding Shock Instabilities

Xu, Stone, & Hardee (1995) have studied the Kelvin-Helmholtz (K-H) instability in the beam of cooling jets to examine if it can be responsible for some of the helical patterns and dense knots found inside these jets. Such a K-H model may well apply to R Aqr at some level, but our simple isothermal-shock model does not address such issues. We have attempted to categorize the spatial features of the R Aqr jet in terms of a dynamical model to account for the helical structure (Koupelis & Van Horn 1988) seen in the ultraviolet and enhanced ejection at periastron to account for the seeming dense emission knots, particularly in the radio. More importantly, we do not observe signs of instabilities (e.g., filamentary structures) along the entire leading edge of the jet. It remains to be seen if such structures exist on a scale smaller than present observations (see § 2) afford.

4.5. Angular Momentum of a Path-oriented jet

The variable nature of the Mira LPV in the R Aqr system was first detected in 1811 (Harding 1816), and the system has been under scrutiny since that time. Its large-scale nebulosity was first discovered in 1921 (Lampland 1923a, 1923b). Mira variables are the endpoints in asymptotic giant branch evolution just prior to planetary nebula formation and their limited lifetimes are variously estimated from about 50,000 to 300,000 yr (Whitelock 1990). With the advent of the jet that was first noticed above the background of the large-scale nebulosity circa 1977 (Wallerstein & Greenstein 1980; Herbig 1980), we are obviously privileged to witness R Aqr in a relatively brief phase of its systemic development. With that in mind, we consider the angular momentum aspects of our path-oriented jet. Using equation (9) at our assumed distance of 250 pc, we calculate that the total angular momentum (J) of the observable NE radio jet is $J_{\text{JET}} \sim 2 \times 10^{51} \text{ g cm}^2 \text{ s}^{-1}$, assuming that the conical jet rotates on the sky at $\sim 0.5 \text{ yr}^{-1}$. Neglecting negligible contributions from the accretion disk and stellar rotation, the total angular momentum from binary orbital motion is $J_B \sim 2.4 \times 10^{53} \text{ g cm}^2 \text{ s}^{-1}$ for $e \geq 0.8$, an LPV mass of $1.75 M_\odot$, and a secondary mass of $1 M_\odot$. Consistent with observations (see, e.g., Lehto & Johnson 1992; Hollis & Michalitsianos 1993), our model shows that the jet age (A) must be ≥ 100 yr. Therefore, the jet acquires angular momentum at a rate $J_{\text{JET}}/A \leq 2 \times 10^{49} \text{ g cm}^2 \text{ s}^{-1} \text{ yr}^{-1}$, suggesting the removal of all the systemic angular momentum in $J_B \times A/J_{\text{JET}} \geq 12,000$ yr, assuming that the present state of the jet continues. Such an angular momentum time-scale seems reasonable, given that the jet appears to be a recent advent within a binary system containing a primary in an ephemeral phase of stellar evolution. If the system is undergoing a severe loss of angular momentum, it would drastically alter the binary system and may even stop the jet. Fortunately, it is now possible to observe the apparent orbit of R Aqr with high-resolution 7 mm VLA observations (Hollis, Pedelty, & Lyon 1997), so this aspect of the angular momentum question can, in principle, be observationally tested over time.

5. SUMMARY

Our 6 cm VLA observations show that the R Aqr jet has undergone a lateral rotation of $\sim 6^\circ$ – 12° on the plane of the sky between 1982 and 1995, and 1994 *HST*/FOC imagery at $\sim 2330 \text{ \AA}$ shows that ultraviolet emission lies along the

leading edge of the rotating radio jet. We used proper-motion data in both the radio and ultraviolet and radial velocity data from optical studies to determine the space-velocity and acceleration-magnitude relationships of the jet material. The dichotomy in these observed magnitude relationships at disparate wavelengths constrain us to assume that a path-oriented jet is appropriate. We believe that a path-oriented jet as dictated by the proper-motion observations and further supported by the apparent lateral rotation of the jet over the course of the last 13.2 yr is one of the more interesting aspects of this current work. We have not offered an explanation for this effect, but such a model could reflect powerful, large-scale magnetic field lines emanating from a rotating hot companion and its accretion disk. The important result is that we may have the first observational evidence for a path-oriented jet rather than the usually assumed garden hose model with constituent particles or parcels experiencing independent trajectories.

To model the jet emission as consisting of plane-parallel isothermal shocks along the leading edge of rotation, we used the velocity-magnitude relationships for the ultraviolet and radio material and the condition of mass conservation along the conical jet to obtain the physical parameters (T , P , n) as a function of distance s relative to the LPV. The ultraviolet-emitting region is consistent with the adiabatic region of the radiating shock in the form of a high-temperature, low-density sheath that surrounds the post-shock radio-emitting cone at $\sim 10^4 \text{ K}$. The explanation we favor is that the jet is a rotating collimated path laterally encountering ambient circumstellar material previously ejected in a well-documented outburst that occurred ~ 660 yr ago. The path itself may well be a result of precession of the accretion disk that surrounds a rotating hot companion that probably anchors a large-scale magnetic field, giving rise to the collimated jet. Integration of the radio density function within the bicone yields a total jet mass of $\sim 3.1 \times 10^{-5} M_\odot$, which, when compared to the estimate of the mass loss of $\sim 2.7 \times 10^{-7} M_\odot \text{ yr}^{-1}$, provides an estimated age of 115 yr in agreement with the observed (kinematically determined) age of the oldest radio jet components.

We conclude that our model is self-consistent in three observationally verifiable aspects: agreement with previously published electron densities of jet features (Hollis et al. 1985; Kafatos, Michalitsianos, & Hollis 1986); agreement with previously published velocities of jet features (Lehto & Johnson 1992; Hollis & Michalitsianos 1993; Hollis et al. 1997); and agreement with previously published ages of the oldest jet components (Lehto & Johnson 1992; Hollis & Michalitsianos 1993). While we have shown that the physical parameters of the model (temperature, density, velocity, and mass and age of the jet) favorably compare to previously published observations, the rate of angular momentum acquired by such a jet model at the expense of orbital angular momentum is shown to be problematic. However, the effect of the jet on the apparent binary orbit can now, in principle, be observationally tested over time.

We thank E. Seaquist for critical comments on an early version of the manuscript, and B. Draine, S. Shore, S. Zalesak, and an anonymous referee for useful comments and discussions regarding the shock model. We appreciate the help of Judith Laue with graphic arts. J. M. H. and J. A. P. received support from NASA RTOP 344-02-03-01.

REFERENCES

- Bridle, A. H., & Perley, R. A. 1984, *ARA&A*, 22, 319
 Clark, B. G. 1981, *A&A*, 89, 377
 Cornwell, T. J., & Braun, R. 1989, in *Synthesis Imaging in Radio Astronomy*, ed. R. A. Perley, F. R. Schwab, & A. H. Bridle (San Francisco: ASP), 167
 Dyson, J. E., & Williams, D. A. 1980, in *Physics of the Interstellar Medium* (New York: John Wiley & Sons), 106
 Harding, K. 1816, *Z. Astrophys.*, 1, 449
 Haynes, R. F., Lerche, I., & Wright, A. E. 1980, *A&A*, 81, 83
 Herbig, G. 1980, *IAU Circ.* 3535
 Hinkle, K. H., Wilson, T. D., Scharlach, W. W. G., & Fekel, F. C. 1989, *AJ*, 98, 1820
 Hollis, J. M., Dorband, J. E., & Yusef-Zadeh, F. 1992, *ApJ*, 386, 293
 Hollis, J. M., Kafatos, M., Michalitsianos, A. G., & McAlister, H. A. 1985, *ApJ*, 289, 765
 Hollis, J. M., Kafatos, M., Michalitsianos, A. G., Oliversen, R. J., & Yusef-Zadeh, F. 1987, *ApJ*, 321, L55
 Hollis, J. M., Lyon, R. G., Dorband, J. E., & Feibelman, W. A. 1997, *ApJ*, 475, 231
 Hollis, J. M., & Michalitsianos, A. G. 1993, *ApJ*, 411, 235
 Hollis, J. M., Oliversen, R. J., Kafatos, M., Michalitsianos, A. G., & Wagner, R. M. 1991, *ApJ*, 377, 227
 Hollis, J. M., Pedelty, J. A., & Lyon, R. G. 1997, *ApJ*, 482, L85
 Kafatos, M., Hollis, J. M., & Michalitsianos, A. G. 1983, *ApJ*, 267, L103
 Kafatos, M., & Michalitsianos, A. G. 1982, *Nature*, 298, 540
 Kafatos, M., Michalitsianos, A. G., & Hollis, J. M. 1986, *ApJS*, 62, 853
 Kouvelis, T., & Van Horn, H. M. 1988, *ApJ*, 324, 93
 Lampland, C. O. 1923a, *Pub. Am. Astron. Soc.*, 4, 319
 _____, 1923b, *Pub. Am. Astron. Soc.*, 4, 365
 Leahy, D. A., & Taylor, A. R. 1987, *A&A*, 176, 262
 Lehto, H. J., & Johnson, D. R. H. 1992, *Nature*, 355, 705
 Michalitsianos, A. G., Kafatos, M., & Hobbs, R. W. 1980, *ApJ*, 237, 506
 Michalitsianos, A. G., Oliversen, R. J., Hollis, J. M., Kafatos, M., Crull, H. E., & Miller, R. J. 1988, *AJ*, 95, 1478
 Nota, A., Jedrzejewski, R., & Hack, W. 1995, *The Faint Object Camera Instrument Handbook, Version 6.0* (Baltimore: Space Telescope Science Institute)
 Omont, A. 1991, in *Late Stages of Stellar Evolution/Computational Methods in Astrophysical Hydrodynamics*, ed. C. B. de Loore (Berlin: Springer), 161
 Reid, M. J., & Menten, K. M. 1997, *ApJ*, 476, 327
 Schild, H. 1989, *MNRAS*, 240, 63
 Solf, J., & Ulrich, H. 1985, *A&A*, 148, 274
 Spitzer, L. 1978, *Physical Processes in the Interstellar Medium* (New York: Wiley-Interscience)
 Wallerstein, G. 1986, *PASP*, 98, 118
 Wallerstein, G., & Greenstein, J. L. 1980, *PASP*, 92, 275
 Whitelock, P. A. 1987, *PASP*, 99, 573
 _____, 1990, in *ASP Conf. Proc. II, Confrontation Between Stellar Pulsation and Evolution*, ed. C. Cacciari & G. Clementini (San Francisco: ASP), 365
 Willson, L. A., Garnavich, P., & Mattei, J. A. 1981, *Inf. Bull. Variable Stars* 1961
 Xu, J., Stone, J. M., & Hardee, P. E. 1995, *BAAS*, 187, 2103

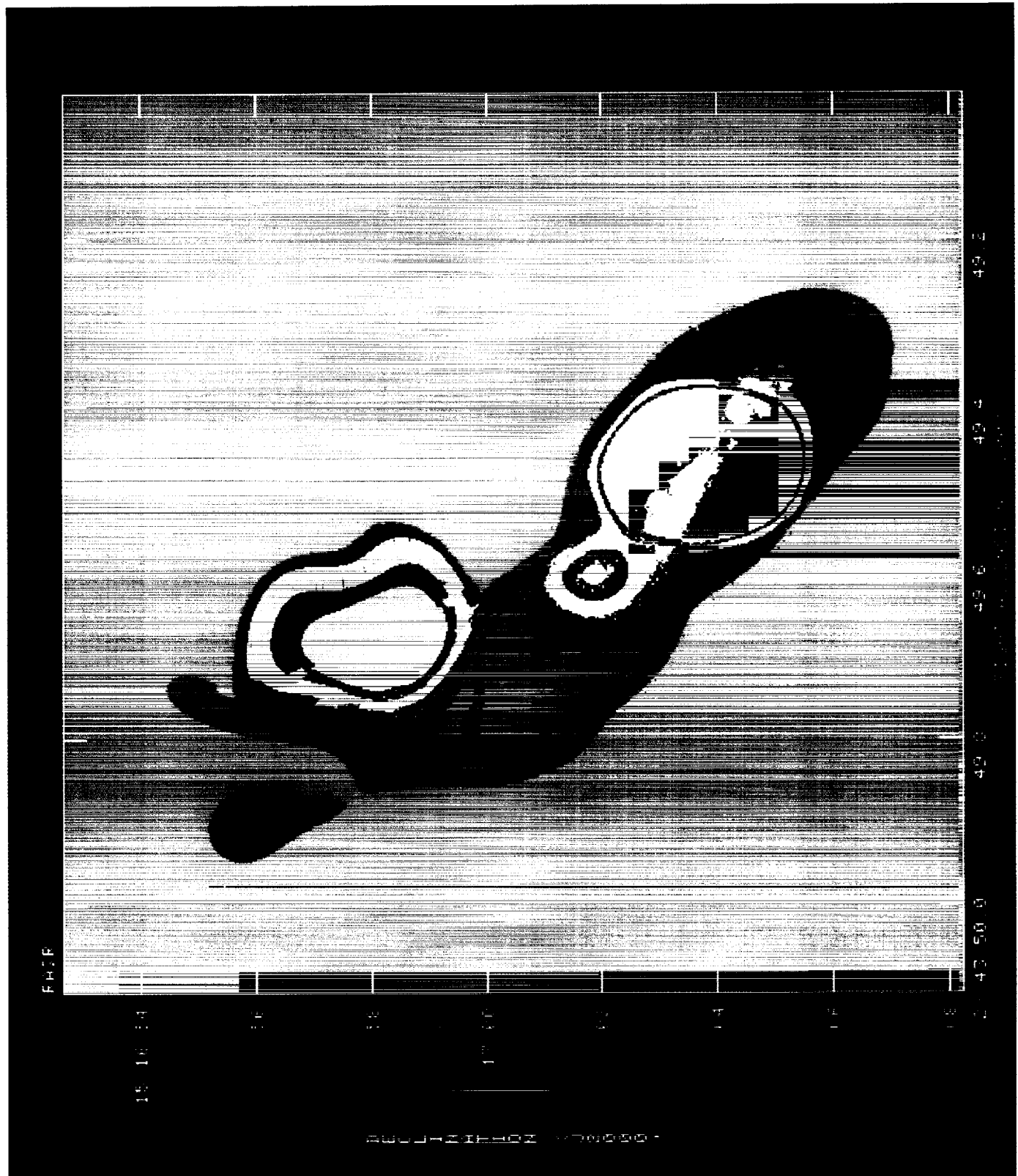


FIG. 1.—Superimposed VLA 6 cm images of the R Aqr jet taken in 1982 (green color) and 1995 (blue color) and an *HST*/FOC ultraviolet image (red color) at $\sim 2330 \text{ \AA}$ obtained in 1994. Note that the color white is produced when all colors combine. Comparison of the VLA images shows that the radio jet has undergone a lateral rotation of $\sim 6^\circ\text{--}12^\circ$ on the plane of the sky. Note that the restoring beam of the radio emission is $1''.67 \times 1''.25$ while the *HST* image is diffraction limited ($\sim 0''.2$ diameter core encompassing $\sim 70\%$ of the energy for a point source). The *HST* image is a better estimate of the true morphology of the R Aqr jet. See Fig. 2 to compare the 1994 *HST* image with the 1995 radio emission at the same resolution.

